# Reverse Shape Memory Effect Related to $\alpha \rightarrow \gamma$ Transformation in a Fe-Mn-Al-Ni Shape Memory Alloy

HUABEI PENG, PAN HUANG, TIANNAN ZHOU, SHANLING WANG, and YUHUA WEN

In this study, we investigated the shape memory behavior and phase transformations of solution-treated $Fe_{43.61}Mn_{34.74}Al_{13.38}Ni_{8.27}$ alloy between room temperature and 1173 K (900 °C). This alloy exhibits the reverse shape memory effect resulting from the phase transformation of $\alpha$ (bcc) $\rightarrow \gamma$ (fcc) between 673 K and 1073 K (400 °C and 800 °C) in addition to the shape memory effect resulting from the martensitic reverse transformation of $\gamma'$ (fcc) $\rightarrow \alpha$ (bcc) below 673 K (400 °C). There is a high density of hairpin-shaped dislocations in the $\alpha$ phase undergoing the martensitic reverse transformation of $\gamma' \rightarrow \alpha$. The lath $\gamma$ phase, which preferentially nucleates and grows in the reversed $\alpha$ phase, has the same crystal orientation with the reverse-transformed $\gamma'$ martensite. However, the vermiculate $\gamma$ phase, which is precipitated in the $\alpha$ phase between lath $\gamma$ phase, has different crystal orientations. The lath $\gamma$ phase is beneficial to attaining better reverse shape memory effect than the vermiculate $\gamma$ phase.

## I. INTRODUCTION

SHAPE memory alloys have attracted much attention due to their shape memory effect and super-elasticity.[1–3] Various shape memory alloys, such as Ti-Ni-based, Cu-based, Fe-based, and Ni-based alloys, are developed.[4–7] Note that Omori et al. developed a $Fe_{43.5}Mn_{34}Al_{15}Ni_{7.5}$ alloy exhibiting over 8 pct fracture strain and over 5 pct super-elastic strain derived from the $\alpha$ (bcc) to $\gamma'$ (fcc) martensitic transformation and its reverse transformation in 2011.[8] Furthermore, this alloy exhibits super-elasticity over a very wide temperature range from 77 K to 513 K (−196 °C to 240 °C) with smallest temperature dependence of super-elastic stress as compared with other major alloy systems.[8] Thus, it is regarded as a fascinating candidate for large-scale applications.

Recently, a large proportion of studies reported the martensitic transformation and super-elasticity of FeMnAlNi shape memory alloys. Kwon et al. added Cr element into a $Fe_{35.18}Mn_{30.58}Al_{26.7}Ni_{5.7}Cr_{1.85}$ alloy and found that this alloy undergoes $\alpha \rightarrow \varepsilon \rightarrow \gamma'$ martensitic transformation during deformation.[9] Omori et al. indicated that the thermoelastic $\alpha/\gamma'$ martensitic transformation is associated with the precipitation of nano-sized coherent B2 phase in the $Fe_{43.5}Mn_{34}Al_{15}Ni_{7.5}$ alloy.[10] Furthermore, Omori et al. reported that a super-elastic strain of about 5 pct is obtained as the ratio of wire diameter to mean grain diameter exceeds one for $Fe_{43.5}Mn_{34}Al_{15}Ni_{7.5}$ alloy wires with a $\langle 110 \rangle$ fiber texture.[11] Tseng et al. found that the super-elastic strain under compression is higher than that under tension for the aged single crystalline $Fe_{43.5}Mn_{34}Al_{15}Ni_{7.5}$ alloy oriented along the [100] direction.[12] In addition, they also indicated that the same alloy shows the optimal super-elastic properties under compression along the [100] direction since precipitating the B2 phase with the diameter of around 6 to 10 nm.[13] Besides, Vollmer et al. mentioned that cracks mainly linked to grain boundaries of $\alpha$ phase would appear since the polycrystalline $Fe_{43.5}Mn_{34}Al_{15}Ni_{7.5}$ alloy was rapidly quenched into cold water after solution treatment.[14] They pointed out that precipitating the ductile $\gamma$ phase at the grain boundaries of $\alpha$ phase through slowing the cooling rate after solution treatment is able to suppress the crack formation.[14] In the term of the shape memory effect of FeMnAlNi alloys, it has been only reported by the patent of Ishida et al. so far.[15]

Here, we present the reverse shape memory effect (RSME) in a $Fe_{43.61}Mn_{34.74}Al_{13.38}Ni_{8.27}$ alloy. By far, to our knowledge, data on the RSME of FeMnAlNi alloys and its mechanism are still lacking in open literature. The RSME, i.e., recovering their deformed shape upon heating to higher temperature after recovering their original shape due to the shape memory effect, has been reported in Cu-Zn-Al shape memory alloys.[16–19] Their RSME is caused by the $\beta'$ (B2) to $\alpha$ (fcc) bainitic transformation,[16–19] while we found that the RSME of $Fe_{43.61}Mn_{34.74}Al_{13.38}Ni_{8.27}$ alloy is related to the phase transformation of $\alpha$ (bcc) $\rightarrow \gamma$ (fcc) in the present paper.

HUABEI PENG, PAN HUANG, and YUHUA WEN are with the College of Manufacturing Science and Engineering, Sichuan University, Chengdu 610065, China. Contact e-mail: wenyh@scu.edu.cn TIANNAN ZHOU is with the College of Polymer Science and Engineering, Sichuan University, Chengdu 610065, China. SHANLING WANG is with the Analytical and Testing Center, Sichuan University, Chengdu 610065, China. Contact e-mail: wangshanling@scu.edu.cn

The application scope of Fe-Mn-Al-Ni alloys will be further expanded due to their reverse shape memory effect.

## II. EXPERIMENTAL

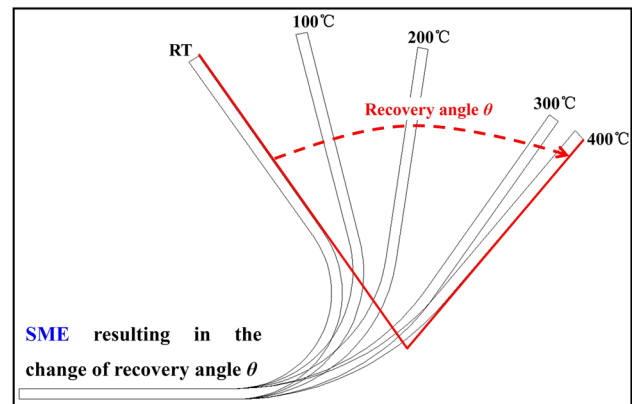The ingot of $Fe_{43.61}Mn_{34.74}Al_{13.38}Ni_{8.27}$ alloy was prepared by induction melting in an argon atmosphere. This ingot was then hot forged at 1473 K (1200 °C) into a plate with 20-mm thickness after being homogenized at 1373 K (1100 °C) for 15 hours. The sheet specimens with 1.5 mm thickness were cut from the plate by electric discharge machining. Next, these sheet specimens were sandwiched between two sheets of 304 austenitic stainless steels and solution treated at 1423 K (1150 °C) for 10 minutes in vacuum, followed by water quenching. For evaluating the shape memory behavior by a bending test, wire specimens with cross-section of 1.5 mm × 2 mm were cut from the solution-treated sheets by electric discharge machining. The procedures of measuring shape memory behavior were as follows: first, the wire specimen was deformed at room temperature (RT) by bending over a mold 30 mm in diameter; second, the bent specimen was annealed in turn to a certain temperature and subsequent air cooling to RT, and the corresponding recovery angle $\theta$ was measured. The heating temperatures were between 373 K and 1173 K (100 °C and 900 °C). The surface strain of bending test was determined by the equation

$$\varepsilon = \frac{t}{2R + t}, \qquad [1]$$

where $\varepsilon$ is the bending strain after unloading; $t$ is the sample thickness; and $R$ is the bending radius after unloading. The bending strain was about 3.4 pct according to Eq. [1]. The color optical etching method was chosen to investigate the microstructures, and the composition of the color etching solution was 1.2 pct $K_2S_2O_5$ + 0.5 pct $NH_4HF_2$ in distilled water. Microstructures were further studied by a Tecnai G2 F20 transmission electron microscope (TEM) and electron backscatter diffraction (EBSD) using a FEI F50 field emission scanning electron microscope (SEM). A step size of 1 and 0.5 $\mu$m was used to scan the deformed and annealed samples for EBSD, respectively. The specimens for TEM were firstly ground mechanically into thin foils of about 80 $\mu$m, punched into circles with a diameter of 3 mm, and then electropolished using a twin jet polisher in a solution of sulphuric acid and methanol (1:4) until a hole appeared in the center. The chemical compositions of different phases were determined by JEOL 8100 electron probe microanalysis (EPMA) instrument. The phases were determined by XRD using a Bruker D8 Advance X-ray diffraction (XRD) apparatus. Phase transformation process was observed by *ex situ* color optical metallographic technique and *in situ* XRD. The *ex situ* color optical micrographs were captured at RT after annealing at each temperature. The *in situ* XRD were measured using
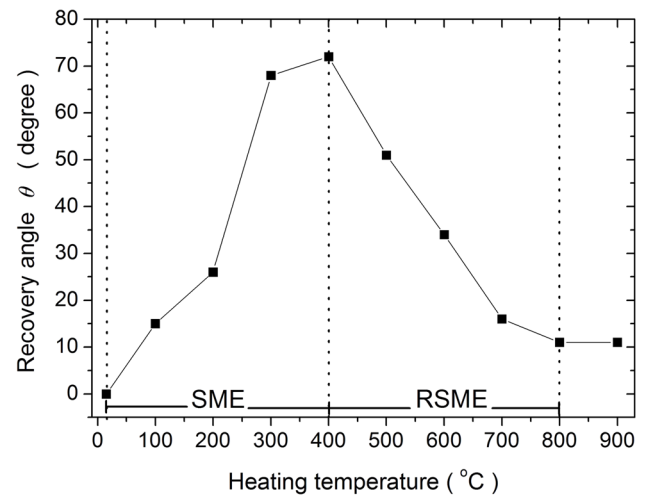


(a)



(b)
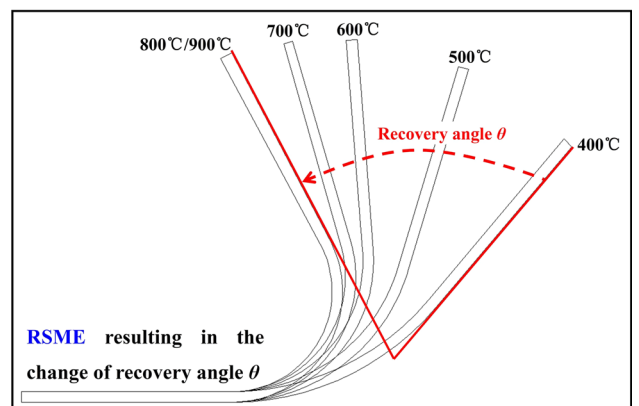


(c)

Fig. 1—Relationship between heating temperatures and recovery angle $\theta$ for solution-treated $Fe_{43.61}Mn_{34.74}Al_{13.38}Ni_{8.27}$ alloy after 3.4 pct bending strain at RT. (*a*) experimental results; (*b*) schematic diagram of shape change resulting from SME; (*c*) schematic diagram of shape change resulting from RSME.

a Bruker D8 Discover X-ray diffraction with a two-dimension detector VANTEC 500 and a heating stage Anton Paar DHS 1100, and the heating rate was 50 °C/min.
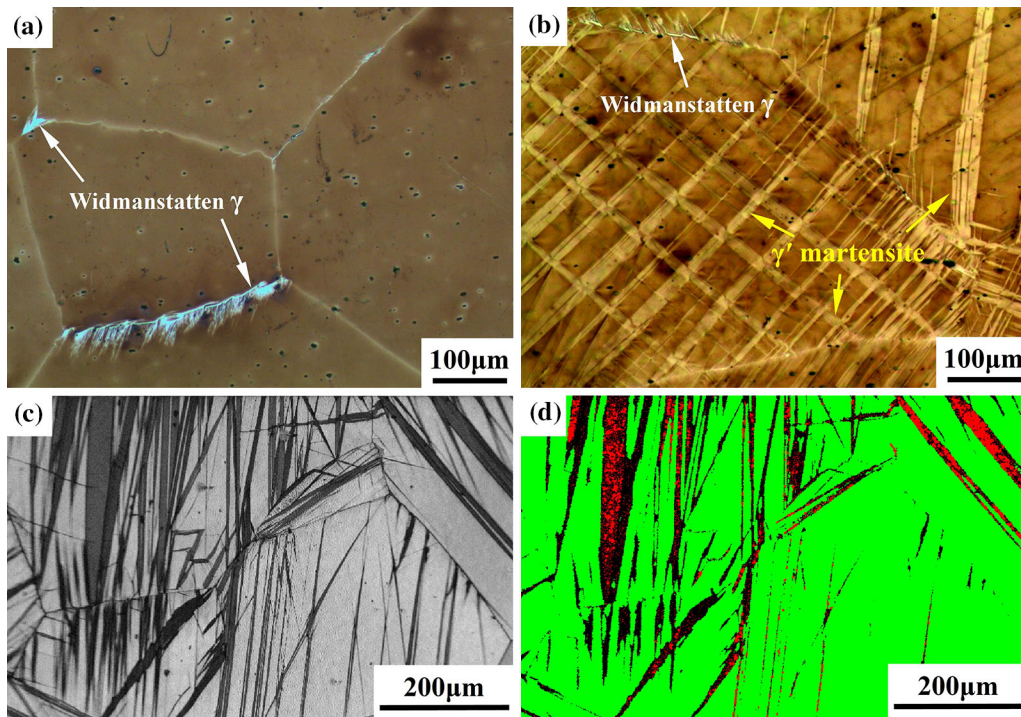
Fig. 2—Color optical micrographs of solution-treated $Fe_{43.61}Mn_{34.74}Al_{13.38}Ni_{8.27}$ alloy (*a*) and one after 2.5 pct deformation strain at RT (*b*). EBSD results of solution-treated $Fe_{43.61}Mn_{34.74}Al_{13.38}Ni_{8.27}$ alloy after 2.5 pct deformation strain at RT: (*c*) image quality map; (*d*) phase map, red areas are $\gamma'$ martensite while green areas are $\alpha$ phase.
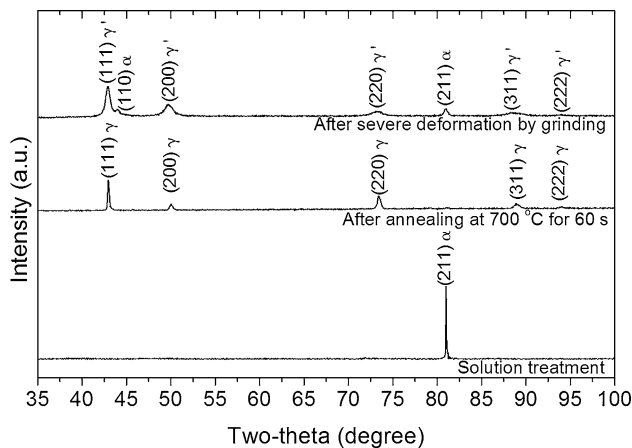


Fig. 3—XRD patterns of solution-treated $Fe_{43.61}Mn_{34.74}Al_{13.38}Ni_{8.27}$ alloy before and after annealing at 973 K (700 °C) for 60 s or severe deformation by grinding to induce $\gamma'$ martensite in the surface.

## III. RESULTS AND DISCUSSION

### A. *Shape Memory Behavior*

Figure 1 gives the recovery angle $\theta$ as a function of heating temperatures for solution-treated $Fe_{43.61}Mn_{34.74}Al_{13.38}Ni_{8.27}$ alloy after 3.4 pct bending strain at RT. When the heating temperature was below 673 K (400 °C), the $\theta$ increased gradually to 72 deg as increasing the temperatures, which is referred to as the shape memory effect. Above 673 K (400 °C), however, the $\theta$ gradually decreased to 11 deg with increasing the temperatures up to 1073 K (800 °C). In other words,

the shape moved toward the deformed shape, *i.e.*, revealing the RSME. And further increasing the heating temperature to 1173 K (900 °C), $\theta$ had no change. Note that the RSME of solution-treated $Fe_{43.61}Mn_{34.74}Al_{13.38}Ni_{8.27}$ alloy appeared in the temperature range from 673 K and 1073 K (400 °C and 800 °C).

### B. *Microstructure Evolution Before and After Annealing*

For solution-treated $Fe_{43.61}Mn_{34.74}Al_{13.38}Ni_{8.27}$ alloy, some white Widmanstatten $\gamma$ phase grew from some grain boundaries (Figure 2(a)). Omori *et al.* indicated that some amount of $\gamma$ phase is precipitated mainly along grain boundaries of $\alpha$ phase during cooling after the solution treatment or is precipitated in $\alpha$ phase matrix at a solution treatment.[15] In Fe-Mn-Al alloys, Widmanstatten $\gamma$ phase is precipitated along the grain boundaries of $\alpha$ phase during cooling after the solution treatment due to insufficient cooling rate,[20] while island-like $\gamma$ phase is generally precipitated by solution treated at the phase region of $\alpha + \gamma$.[20,21] Therefore, the Widmanstatten $\gamma$ phase in solution-treated $Fe_{43.61}Mn_{34.74}Al_{13.38}Ni_{8.27}$ alloy was precipitated during cooling because the cooling rate of water quenching was not enough to suppress the precipitation of $\gamma$ phase. After 2.5 pct deformation at RT, the lath $\gamma'$ martensite was induced in solution-treated $Fe_{43.61}Mn_{34.74}Al_{13.38}Ni_{8.27}$ alloy (Figures 2(b) through (d)). Note that only $\alpha_{211}$ peak appears in the XRD patterns of solution-treated $Fe_{43.61}Mn_{34.74}Al_{13.38}Ni_{8.27}$ alloy because its grain size is coarse (Figure 3). In order to obtain the lattice parameter of the $\gamma'$ martensite, we severely deformed the
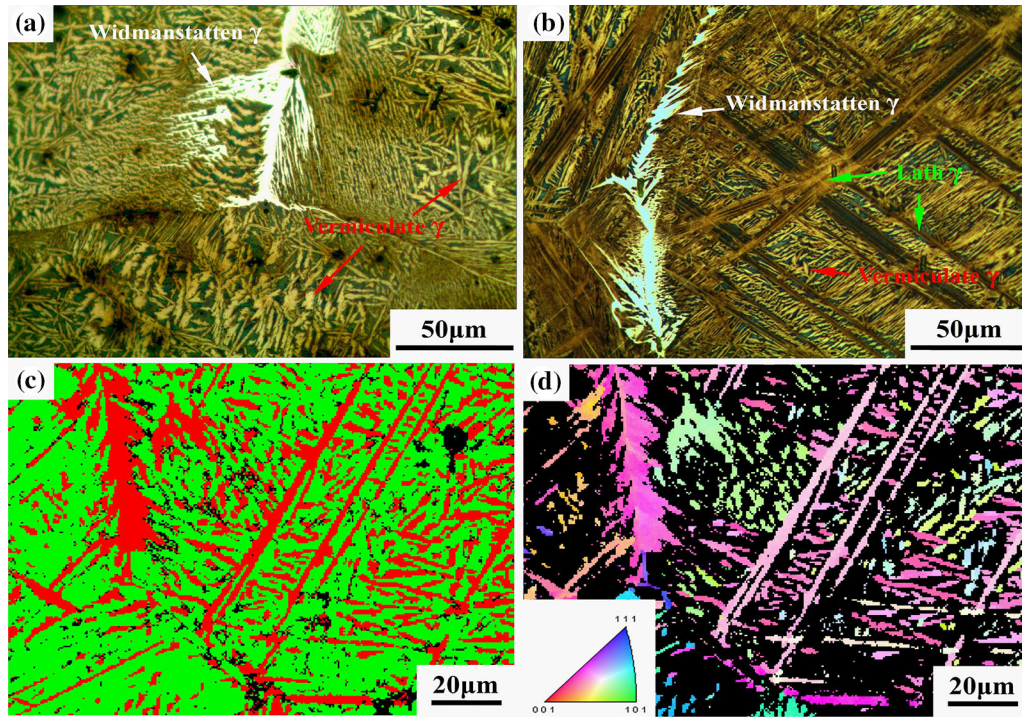
Fig. 4—Solution-treated $Fe_{43.61}Mn_{34.74}Al_{13.38}Ni_{8.27}$ alloy subjected to annealing at 973 K (700 °C) for 60 s (*a*) as well as one subjected to annealing at 973 K (700 °C) for 60 s after 2.5 pct deformation strain at RT (*b* to *d*). (a) and (b) are color optical micrographs; (*c*) is EBSD phase map, red areas are $\gamma$ phase while green areas are $\alpha$ phase; (d) is colored orientation map and corresponding inverse pole figure of $\gamma$ phase.

**Table I. EPMA Measured Chemical Compositions of Different Phases in Solution-Treated $Fe_{43.61}Mn_{34.74}Al_{13.38}Ni_{8.27}$ Alloy After 2.5 Pct Deformation Strain at RT and Subsequent Annealing at 973 K (700 °C) for 60 s**

| | Elements (Wt Pct) | | | |
| --- | --- | --- | --- | --- |
| Phases | Fe | Mn | Al | Ni |
| Lath $\gamma$ phase | bal. | 37.72 | 5.29 | 9.32 |
| Vermiculate $\gamma$ phase | bal. | 37.93 | 5.54 | 9.74 |
| $\alpha$ phase | bal. | 35.98 | 6.68 | 9.36 |

sample of solution-treated $Fe_{43.61}Mn_{34.74}Al_{13.38}Ni_{8.27}$ alloy by grinding to induce $\gamma'$ martensite in the surface. The XRD results show that the lattice parameter of the $\gamma'$ martensite was 0.3651 nm.

When solution-treated $Fe_{43.61}Mn_{34.74}Al_{13.38}Ni_{8.27}$ alloy was annealed at 973 K (700 °C) for 60 seconds, lots of yellow vermiculate phase was precipitated in blue $\alpha$ phase (Figure 4(a)). The XRD results indicate that the vermiculate phase is $\gamma$ phase, and its lattice parameter is 0.3646 nm, which is very close to the lattice parameter of $\gamma'$ martensite (Figure 3). In this case, the RSME of solution-treated $Fe_{43.61}Mn_{34.74}Al_{13.38}Ni_{8.27}$ alloy may be related to the phase transformation of $\alpha \rightarrow \gamma$. For deformed $Fe_{43.61}Mn_{34.74}Al_{13.38}Ni_{8.27}$ alloy, some lath yellow phase appears in blue $\alpha$ phase in addition to yellow vermiculate $\gamma$ phase after 973 K (700 °C) annealing for 60 seconds (Figure 4(b)). We determined the chemical compositions of vermiculate $\gamma$ phase and lath phase as well as $\alpha$ phase, as shown in Table I. The vermiculate $\gamma$ phase and lath phase have almost the same chemical compositions. Therefore, the lath phase should

be $\gamma$ phase. The EBSD results further indicated that the lath phase was $\gamma$ phase (Figures 4(c) and (d)). Note that the morphology of lath $\gamma$ phase is similar with that of $\gamma'$ martensite. Accordingly, the lath $\gamma$ phase may be derived from the residual $\gamma'$ martensite which did not transform back to $\alpha$ phase, or may be the new phase that nucleated and grew in the reversed $\alpha$ phase undergoing the martensitic reverse transformation of $\gamma' \rightarrow \alpha$.

### C. *Phase Evolution of Deformed Alloy During Annealing*

In order to clarify the formation process of lath and vermiculate $\gamma$ phase, we used *ex situ* color optical metallographic technique (Figure 5) and *in situ* XRD (Figure 6) to determine the phase transformation process of deformed $Fe_{43.61}Mn_{34.74}Al_{13.38}Ni_{8.27}$ alloy during annealing. When the alloy was annealed at 673 K (400 °C), some $\gamma'$ martensite transformed back to the $\alpha$ phase and some residual $\gamma'$ martensite retained (Figure 5). The XRD results are similar with the results of color optical micrographs. The diffraction spot of $\gamma'$
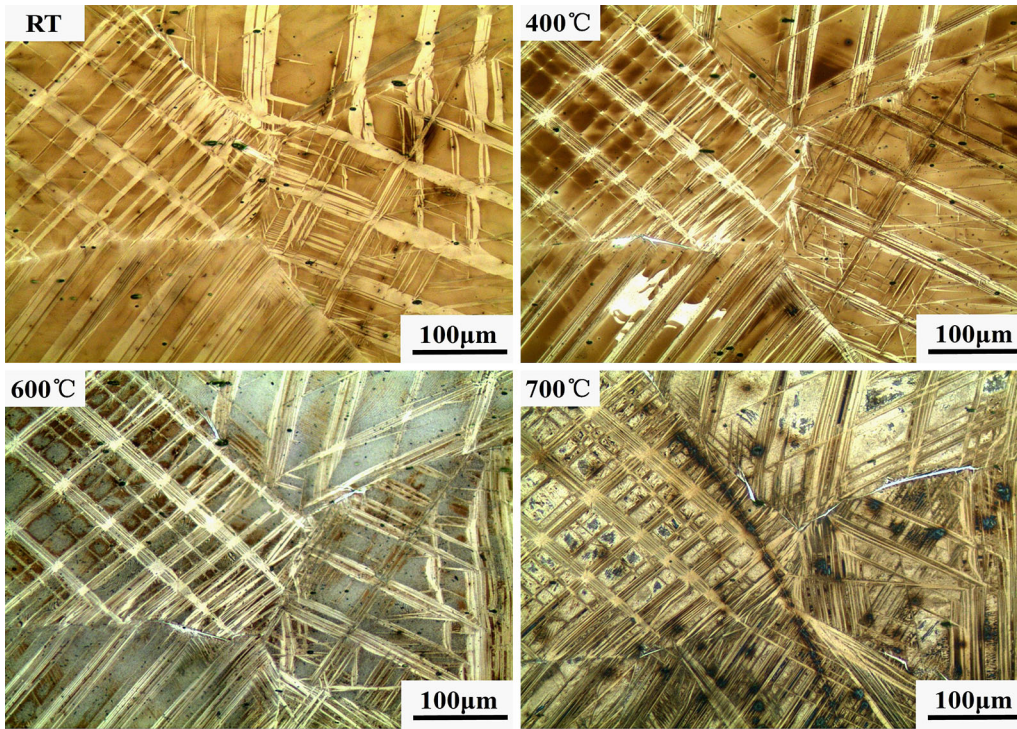
Fig. 5—*Ex situ* color optical micrographs of solution-treated $Fe_{43.61}Mn_{34.74}Al_{13.38}Ni_{8.27}$ alloy subjected to 2.5 pct deformation strain at RT and subsequent annealing in turn at different temperatures for 60 s, respectively. For the purpose of observing almost the same area as far as possible, the sample had to be etched slightly. In this case, some microstructure details cannot be revealed.
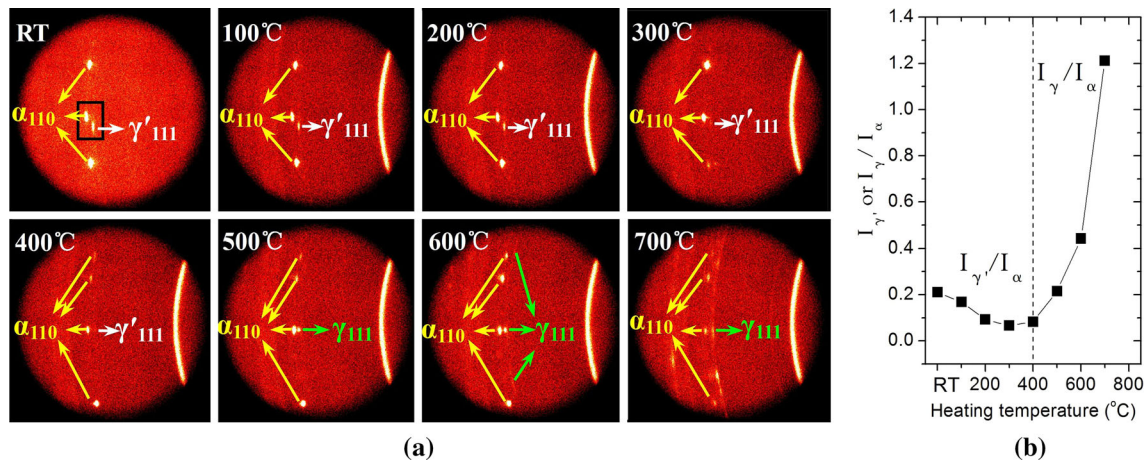


Fig. 6—(*a*) *In situ* XRD patterns of solution-treated $Fe_{43.61}Mn_{34.74}Al_{13.38}Ni_{8.27}$ alloy subjected to 2.5 pct deformation strain at RT and subsequent heating up to different temperatures, respectively, at heating rate of 50 °C/min. (*b*) Change in the ratios of the integrated intensities of $\gamma'_{111}$ or $\gamma_{111}$ to $\alpha_{110}$ in the same area indicated by black box in Fig. 6(a).

martensite became weaker and weaker with increasing the heating temperatures from RT to 673 K (400 °C) (Figure 6(a)). Thus, the phase transformation of $\gamma' \rightarrow \alpha$ happened below 673 K (400 °C), and some residual $\gamma'$ martensite did not transform back to the $\alpha$ phase when the heating temperature reached 673 K (400 °C). As the alloy was annealed at 873 K (600 °C), a lot of lath $\gamma$ phase was precipitated and occupied the areas in which

the $\gamma'$ martensite had transformed back to the $\alpha$ phase (Figure 5). The XRD results shows that the diffraction spot, which is attributed to $\gamma'$ martensite, became strong clearly when the heating temperature was further increased to 773 K (500 °C) (Figure 6(a)). In fact, according to the results of Figure 5, the strong diffraction spot results from the phase transformation of $\alpha \rightarrow \gamma$. Thus, the $\gamma$ phase is stable when the temperature
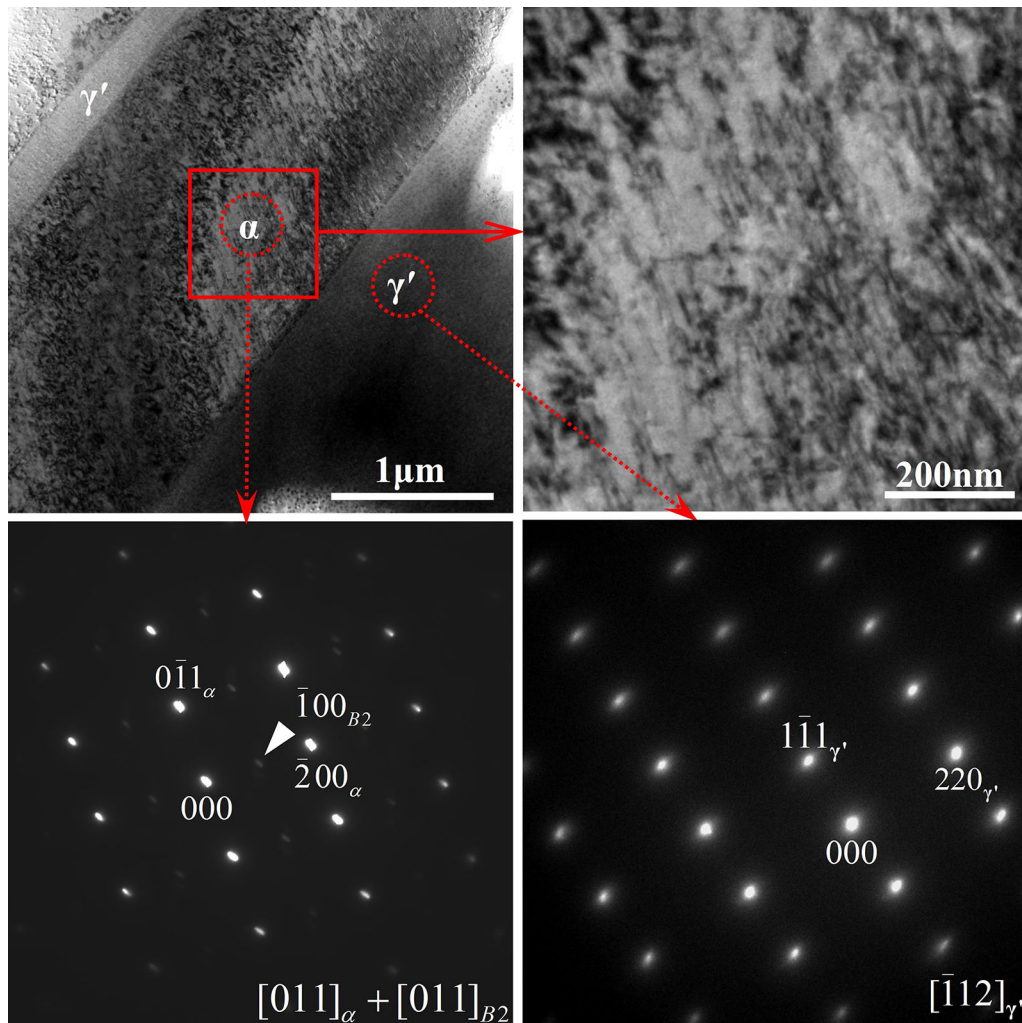
Fig. 7—TEM micrograph and their corresponding selected area electron diffraction patterns of solution-treated $Fe_{43.61}Mn_{34.74}Al_{13.38}Ni_{8.27}$ alloy after 2.5 pct deformation at RT and subsequent annealing at 573 K (300 °C) for 60 s.

is above 673 K (400 °C). As a result, this diffraction spot was attributed to $\gamma$ phase, so it further confirmed that the new lath $\gamma$ phase preferentially nucleates and grows in the reversed $\alpha$ phase and has the same crystal orientation with the reverse-transformed $\gamma'$ martensite. Since the heating temperature was increased to 873 K (600 °C), the same diffraction spot attributed to $\gamma$ phase became stronger, and some diffraction arcs appeared (Figure 6(a)). It is indicated that more $\gamma$ phase, which has the same crystal orientation with the reverse-transformed $\gamma'$ martensite, was precipitated, while a small quantity of $\gamma$ phase with other crystal orientations was also precipitated. Based on the result of *ex situ* color optical micrographs and *in situ* XRD, it is concluded that the lath $\gamma$ phase consisted of the $\gamma$ phase transforming from the residual $\gamma'$ martensite which did not transform back to the $\alpha$ phase and the new $\gamma$ phase which was precipitated during annealing. Further increasing the annealing temperature to 973 K (700 °C), the $\gamma$ phase was precipitated in the $\alpha$ phase between lath $\gamma$ phase (Figure 5). In addition, the XRD

results shows that the diffraction ring attributed to $\gamma$ phase formed (Figure 6(a)), and the ratio of the integrated intensities of $\gamma_{111}$ to $\alpha_{110}$ became much higher at 973 K (700 °C) than at 873 K (600 °C) (Figure 6(b)). It means that much more $\gamma$ phase with different crystal orientations from the reverse-transformed $\gamma'$ martensite was precipitated. The EBSD result also indicates that these $\gamma$ phase exhibited different crystal orientations in Figure 4(d).

### D. *Microstructure After Reverse $\alpha \rightarrow \gamma'$ Martensitic Transformation*

For deformed $Fe_{43.61}Mn_{34.74}Al_{13.38}Ni_{8.27}$ alloy, there is a high density of hairpin-shaped dislocations in the reversed $\alpha$ phase undergoing the martensitic reverse transformation of $\gamma' \rightarrow \alpha$ after annealing at 573 K (300 °C) (Figure 7). This kind of dislocations was also observed in Fe-Ni-C, Fe-Pt, and Fe-Ni-Co-Ti alloys undergoing the reverse fcc/bct martensitic transformation.[22] Kajiwara indicated that the hairpin-shaped

dislocations are formed in the reversed austenite only in the case with a large thermal hysteresis, while very few dislocations are formed in the reversed austenite for the case of a small thermal hysteresis.[22] In this case of a small thermal hysteresis, the martensitic transformation behavior becomes thermoelastic and a good shape memory effect is obtained.[22–24] The hairpin-shaped dislocations are reported to be negatively impact of the mobility of the martensite-austenite interface and their presence may lead to the martensite to be pinned.[12,25] For an aged single crystalline $Fe_{43.5}Mn_{34}Al_{15}Ni_{7.5}$ alloy oriented along the [100] direction under tension, Tseng *et al.* found that the hairpin-shaped dislocations generated during phase transformation pin the $\gamma'$ martensite to prevent it from transforming back to the $\alpha$ phase.[12] Accordingly, the finishing reverse-transformation temperature of $\gamma'$ martensite exceeded 673 K (400 °C) due to the pinning effect of hairpin-shaped dislocations for $Fe_{43.61}Mn_{34.74}Al_{13.38}Ni_{8.27}$ alloy. Note that the above results of *in situ* XRD showed that the $\gamma$ phase was stable as the temperature was above 673 K (400 °C) (Figure 6(a)). Therefore, although further increasing the annealing temperature, the residual $\gamma'$ martensite could not transform back to the $\alpha$ phase and only became the $\gamma$ phase because they have same crystal structure and almost same lattice parameters. Accordingly, the deformed $Fe_{43.61}Mn_{34.74}Al_{13.38}Ni_{8.27}$ alloy did not completely recovery its original shape due in large part to the incomplete reverse transformation of $\gamma'$ martensite (Figure 1). In addition, new phases preferentially nucleate and grow at defects, *i.e.*, $\varepsilon$ martensite preferentially nucleates and grows at the stacking faults in Fe-Mn-Si-based shape memory alloys.[22,26] Therefore, the lath $\gamma$ phase preferentially nucleates and grows in the reversed $\alpha$ phase containing the high density of hairpin-shaped dislocations (Figures 5 and 6). Furthermore, the lath $\gamma$ phase has almost same crystal orientation of the reverse-transformed $\gamma'$ martensite, while lots of vermiculate $\gamma$ phase have different crystal orientations from the reverse-transformed $\gamma'$ martensite (Figures 4(d) and 6). The reason for this result may also be related to the high density of hairpin-shaped dislocations in the reversed $\alpha$ phase.

### E. *Origin of Reverse Shape Memory Effect*

Based on the above results, it is concluded that the RSME is related to the phase transformation of $\alpha \rightarrow \gamma$ for solution-treated $Fe_{43.61}Mn_{34.74}Al_{13.38}Ni_{8.27}$ alloy. When the heating temperatures were between 673 K and 973 K (400 °C and 700 °C), both RSME and $\alpha \rightarrow \gamma$ transformation appeared (Figures 1, 5 and 6). As the recovery temperatures were between 673 K and 873 K (400 °C and 600 °C), the lath $\gamma$ phase preferentially nucleated and grew in the reversed $\alpha$ phase containing the high density of hairpin-shaped dislocations (Figures 5 and 7). Furthermore, they have the same crystal orientation with the reverse-transformed $\gamma'$ martensite (Figure 6). In other words, the morphology and crystal orientations of lath $\gamma$ phase almost recovered to that of $\gamma'$ martensite after annealing. In this case, the reverse recovery angle reached 38 deg due to the RSME

caused by $\alpha \rightarrow \gamma$ transformation (Figure 1). Since further increasing the annealing temperature to 973 K (700 °C), the vermiculate $\gamma$ phase was precipitated in the $\alpha$ phase between lath $\gamma$ phase and has different crystal orientations (Figures 4, 5, and 6). Thus, although much more vermiculate $\gamma$ phase was precipitated at 973 K (700 °C) than at 873 K (600 °C), the reverse recovery angle was only 18 deg (Figure 1). These results indicate that $\alpha \rightarrow \gamma$ transformation resulting in the lath $\gamma$ phase with the same crystal orientation of the reverse-transformed $\gamma'$ martensite is beneficial to attaining better RSME. Therefore, it is a key condition making the $\gamma$ phase precipitate with the same crystal orientation of the reverse-transformed $\gamma'$ martensite for the purpose of obtaining good RSME.

For Cu-Zn-Al alloys, the RSME is quite different from the usual mechanical behavior of shape memory effect due to the martensitic transformation. This kind of RSME is caused by the $\beta'$ (B2) to $\alpha$ (fcc) bainitic transformation which possesses a diffusion-controlled nature.[16–19] For solution-treated $Fe_{43.61}Mn_{34.74}Al_{13.38}Ni_{8.27}$ alloy, its RSME results from the $\alpha$ (bcc) to $\gamma$ (fcc) transformation which also possesses a diffusion-controlled nature because it proceeds with a compositional change (Table I). In the case of Cu-Zn-Al alloys, the bainite is as the high-temperature phase and has very similar crystal structures, crystallographic orientation relationships, and habit planes with the martensite.[17] For the $Fe_{43.61}Mn_{34.74}Al_{13.38}Ni_{8.27}$ alloy, the high-temperature phase, $\gamma$ phase, also has very similar crystallographic characteristics with the $\gamma'$ martensite. Accordingly, for other alloy systems, the RSME is expected to appear since the high-temperature phase and the martensite have very similar crystallographic characteristics.

### IV. CONCLUSIONS

In the present work, we have investigated the shape memory behavior and phase transformations of solution-treated $Fe_{43.61}Mn_{34.74}Al_{13.38}Ni_{8.27}$ alloy between room temperature and 1173 K (900 °C). This alloy shows the shape memory effect, which results from the martensitic reverse transformation of $\gamma'$ (fcc) $\rightarrow \alpha$ (bcc), as the heating temperatures are below 673 K (400 °C). When the heating temperatures are between 673 K and 873 K (400 °C and 800 °C), it exhibits the RSME resulting from the phase transformation of $\alpha$ (bcc) $\rightarrow \gamma$ (fcc). There is a high density of hairpin-shaped dislocations in the reversed $\alpha$ phase undergoing the martensitic reverse transformation of $\gamma' \rightarrow \alpha$. The lath $\gamma$ phase preferentially nucleates and grows in the reversed $\alpha$ phase. This kind of $\gamma$ phase has the same crystal orientation with the reverse-transformed $\gamma'$ martensite, while the vermiculate $\gamma$ phase precipitated in the $\alpha$ phase between lath $\gamma$ phase has different crystal orientations. The lath $\gamma$ phase is beneficial to attaining better RSME than the vermiculate $\gamma$ phase. Thus, it is expected to improve the RSME by promoting the formation of lath $\gamma$ phase which has the same crystal orientation with the reverse-transformed $\gamma'$ martensite.

## REFERENCES

1. T. Omori and R. Kainuma: *Nature*, 2013, vol. 502, pp. 42–44.
2. Y.T. Song, X. Chen, V. Dabade, T.W. Shield, and R.D. James: *Nature*, 2013, vol. 502, pp. 85–88.
3. K. Otsuka and C.M. Wayman: *Shape Memory Materials*, 1st ed., Cambridge University Press, New York, 1998.
4. R. Kainuma, Y. Imano, W. Ito, Y. Sutou, H. Morito, S. Okamoto, O. Kitakami, K. Oikawa, A. Fujita, T. Kanomata, and K. Ishida: *Nature*, 2006, vol. 439, pp. 957–60.
5. Y. Tanaka, Y. Himuro, R. Kainuma, Y. Sutou, T. Omori, and K. Ishida: *Science*, 2010, vol. 327, pp. 1488–90.
6. T. Omori, T. Kusama, S. Kawata, I. Ohnuma, Y. Sutou, Y. Araki, K. Ishida, and R. Kainuma: *Science*, 2013, vol. 341, pp. 1500–02.
7. S.J. Hao, L.S. Cui, D.Q. Jiang, X.D. Han, Y. Ren, J. Jiang, Y.N. Liu, Z.Y. Liu, S.C. Mao, Y.D. Wang, Y. Li, X.B. Ren, X.D. Ding, S. Wang, C. Yu, X.B. Shi, M.S. Du, F. Yang, Y.J. Zheng, Z. Zhang, X.D. Li, D.E. Brown, and J. Li: *Science*, 2013, vol. 339, pp. 1191–94.
8. T. Omori, K. Ando, M. Okano, X. Xu, Y. Tanaka, I. Ohnuma, R. Kainuma, and K. Ishida: *Science*, 2011, vol. 333, pp. 68–71.
9. E.P. Kwon, S. Fujieda, K. Shinoda, and S. Suzuki: *Procedia Eng.*, 2011, vol. 10, pp. 2214–19.
10. T. Omori, M. Nagasako, M. Okano, K. Endo, and R. Kainuma: *Appl. Phys. Lett.*, 2012, vol. 101, p. 231907.
11. T. Omori, M. Okano, and R. Kainuma: *APL Mater.*, 2013, vol. 1, p. 032103.
12. L.W. Tseng, J. Ma, S.J. Wang, I. Karaman, M. Kaya, Z.P. Luo, and Y.I. Chumlyakov: *Acta Mater.*, 2015, vol. 89, pp. 374–83.
13. L.W. Tseng, J. Ma, B.C. Hornbuckle, I. Karaman, G.B. Thompson, Z.P. Luo, and Y.I. Chumlyakov: *Acta Mater.*, 2015, vol. 97, pp. 234–44.
14. M. Vollmer, C. Segel, P. Krooß, J. Günther, L.W. Tseng, I. Karaman, A. Weidner, H. Biermann, and T. Niendorf: *Scripta Mater.*, 2015, vol. 108, pp. 23–26.
15. K. Ishida, R. Kainuma, I. Ohnuma, T. Omori, and K. Ando: *Fe-Based Shape Memory Alloy and Its Production Method*, USA, 2014, US8815027B2.
16. M.M. Reyhani and P.G. McCormick: *Scripta Metall.*, 1986, vol. 20, pp. 571–74.
17. K. Takezawa and S. Sato: *Trans. Jpn. Inst. Met.*, 1988, vol. 29, pp. 894–902.
18. I.C. Lee and I.S. Chung: *Scripta Metall.*, 1989, vol. 23, pp. 161–66.
19. Z. Li, S. Gong, and M.P. Wang: *J. Alloys Compd.*, 2008, vol. 452, pp. 307–11.
20. W.C. Cheng and C.K. Lai: *Scripta Mater.*, 2006, vol. 55, pp. 783–86.
21. W.C. Cheng and H.Y. Lin: *Mater. Sci. Eng. A*, 2002, vol. 323, pp. 462–66.
22. S. Kajiwara: *Mater. Sci. Eng. A*, 1999, vols. 273–275, pp. 67–88.
23. S. Kajiwara and W.S. Owen: *Met. Trans.*, 1974, vol. 5, pp. 2047–61.
24. T. Kikuchi and S. Kajiwara: *Mater. Trans.*, 1993, vol. 34, pp. 907–18.
25. E.K.H. Salje, H. Zhang, H. Idrissi, D. Schryvers, M.A. Carpenter, X. Moya, and A. Planes: *Phys. Rev. B*, 2009, vol. 80, p. 134114.
26. D.Z. Liu, S. Kajiwara, T. Kikuchi, and N. Shinya: *Philos. Mag. A*, 2003, vol. 83, pp. 2875–97.